A&A, 708, A122 (2026)
https://doi.org/10.1051/0004-6361/202557163

Astronomy & Astrophysics

MIGHTEE H I observations of low surface brightness and ultra-diffuse galaxies in the XMM-LSS field

Elizabeth A. K. Adams[1,2,⋆], Barbara Šiljeg[1,2], Anastasia A. Ponomareva[3,4], Natasha Maddox[5], Pavel E. Mancera Piña[6], Maarten Baes[7], Bradley Frank[8], Marcin Glowacki[9], Matt J. Jarvis[10,11], Sambatriniaina H. A. Rajohnson[12], and Gauri Sharma[13,14,15,16,11]

[1] ASTRON, Netherlands Institute for Radio Astronomy, Oude Hoogeveensedijk 4, 7991, PD, Dwingeloo, The Netherlands
[2] Kapteyn Astronomical Institute, University of Groningen, Postbus 800, 9700 AV Groningen, The Netherlands
[3] Centre for Astrophysics Research, School of Physics, Astronomy and Mathematics, University of Hertfordshire, College Lane, Hatfield AL10 9AB, UK
[4] Astrophysics, Department of Physics, University of Oxford, Keble Road, Oxford OX1 3RH, UK
[5] School of Physics, H.H. Wills Physics Laboratory, Tyndall Avenue, University of Bristol, Bristol BS8 1TL, UK
[6] Leiden Observatory, Leiden University, P.O. Box 9513, 2300 RA Leiden, The Netherlands
[7] Sterrenkundig Observatorium, Krijgslaan 281 S9, B-9000 Gent, Belgium
[8] STFC UK Astronomy Technology Centre, Royal Observatory, Edinburgh, Blackford Hill, Edinburgh EH9 3HJ, UK
[9] Institute for Astronomy, University of Edinburgh, Royal Observatory, Edinburgh EH9 3HJ, UK
[10] Astrophysics, Department of Physics, University of Oxford, Keble Road, Oxford OX1 3RH, UK
[11] Department of Physics and Astronomy, University of the Western Cape, Robert Sobukwe Road, 7535, Bellville Cape Town, South Africa
[12] INAF – Osservatorio Astronomico di Cagliari, Via della Scienza 5, I-09047 Selargius (CA), Italy
[13] University of Strasbourg, CNRS UMR 7550, Observatoire astronomique de Strasbourg, F-67000 Strasbourg, France
[14] SISSA International School for Advanced Studies, Via Bonomea 265, I-34136 Trieste, Italy
[15] QGSKY, INFN-Sezione di Trieste, via Valerio 2, I-34127 Trieste, Italy
[16] IFPU Institute for Fundamental Physics of the Universe, Via Beirut, 2, 34151 Trieste, Italy

Received 9 September 2025 / Accepted 16 January 2026

ABSTRACT

Untargeted neutral hydrogen (H I) surveys are well suited to identifying low surface brightness galaxies (LSBGs) that are gas rich, and they offer a complementary view to optically selected populations. We examined the LSBG population as identified via stellar and gaseous content using the MIGHTEE H I XMM-LSS early science data and the publicly available catalogs of optically identified LSBGs. There is currently little overlap between these datasets, with only three galaxies commonly detected. We performed surface brightness photometry of selected MIGHTEE H I detections to find 29 LSBGs, and 26 of these meet the size requirement ($R_{\rm eff}$ > 1.5 kpc) to be ultra-diffuse galaxies (UDGs). Furthermore, we extracted H I spectra at the location of all optically identified galaxies, placing upper limits on the H I-to-stellar mass ratio in these systems. While the H I-identified population overall tends toward bluer colors, the H I-identified and the optically selected samples mostly overlap in mean effective surface brightness, effective radii, and color. Although it is not straightforward to discern why the H I-identified LSBGs were missed in optical searches, this work highlights the utility of H I surveys in finding these faint systems. The H I-identified LSBGs are gas rich compared to the general H I-selected population. Furthermore, three out of four H I-selected UDGs with available kinematics show no systematic offset from the baryonic Tully-Fisher relation, although we are biased away from sources with low rotational velocities due to the low spectral resolution of the data. This work demonstrates the utility of H I observations for finding and characterizing the low surface brightness Universe.

Key words. galaxies: dwarf – galaxies: general – galaxies: ISM – galaxies: photometry

1. Introduction

Low surface brightness galaxies (LSBGs) have been long known and recognized for their importance in constraining galaxy formation models (e.g., Sandage & Binggeli 1984; Dalcanton et al. 1997; Impey et al. 1988). Interest in the low surface brightness (LSB) universe was reinvigorated with the discovery of thousands of very extended LSBGs in the Coma Cluster, which are referred to as ultra-diffuse galaxies (UDGs) and were characterized by their LSB nature and large effective radii (van Dokkum et al. 2015; Koda et al. 2015; Yagi et al. 2016). The realization, enabled by optical surveys with increased sensitivity, that there was a large population of previously overlooked galaxies spurred observers to search for UDGs and theorists to explain their formation mechanism.

The original identification of UDGs in clusters and their need to survive that environment motivated formation theories where UDGs were "failed" galaxies that lived in massive dark matter halos and were quenched by early infall into the cluster (e.g., Yozin & Bekki 2015). Other work identified the cluster UDGs as a subset of the cluster dwarf galaxy population, with their larger sizes attributable to interactions within the cluster (e.g., Venhola et al. 2017; Conselice 2018; Mancera Piña et al. 2019a; Watkins et al. 2023). At the same time, other models have predicted that UDGs are a natural part of the dwarf galaxy population in the field, for instance, that they are the tail of the high-spin halo population (e.g., Amorisco & Loeb 2016; Rong et al. 2017;

⋆ Corresponding author: adams@astron.nl

Posti et al. 2018; Mancera Piña et al. 2020), they form due to gas outflows from star formation (Di Cintio et al. 2017), or they result from early major mergers or collisions (Wright et al. 2021; Silk 2019). Testing these theories requires identifying UDGs in the field population and connecting them to the cluster population.

When searching for field UDGs in optical surveys, redshifts are generally not available, as by their nature these sources are too faint for most large-scale redshift surveys. Thus, selection criteria are based on surface brightness (distance-independent) and angular size. For example, Greco et al. (2018, hereafter G18) searched the wide layer of the Hyper Suprime-Cam (HSC) Subaru Strategic Program (SSP) for galaxies with an effective radius of $r_{\rm eff} = 2.5{-}14''$ and an average surface brightness within $r_{\rm eff}$ in the g band $\overline{\mu}_{\rm eff,g} > 24.3\,{\rm mag\,arcsec^{-2}}$. Similarly, the team of Systematically Measuring Ultra-diffuse Galaxies (SMuDGEs) looked at the Legacy Surveys to find galaxies with a peak surface brightness of $\mu_{0,g} \geq 24\,{\rm mag\,arcsec^{-2}}$ and $r_{\rm eff} \geq 5.3''$ (Zaritsky et al. 2023). These provided LSBGs, some of which were UDG candidates. However, the UDG classification relies on physical size, in particular $R_{\rm eff} > 1.5$ kpc, and thus it requires a distance estimate. Approaches to estimating distances have included statistically correlating with known overdensities or galaxies with known redshifts (Zaritsky et al. 2022; Greene et al. 2022), focusing on satellite galaxies associated with a host with a known redshift (Li et al. 2023, hereafter L23), or using either the surface brightness fluctuations (Carlsten et al. 2019) or the globular cluster luminosity function (e.g., Román et al. 2019).

Leisman et al. (2017) and Janowiecki et al. (2019) showed that there is a large population of gas-rich UDGs also present in neutral hydrogen (H I) surveys. In fact, these studies found gas-bearing UDGs to be extremely gas rich for their stellar mass, with gas fractions ($M_{\rm HI}/M_*$) of up to 100. An H I detection is completely independent of the stellar content, enabling detection of galaxies that might be missed in optical searches due to insufficient sensitivity or biases in detection methods (e.g., due to shredding). Hence, it provides a complementary view to optical searches for LSBGs and UDGs.

In addition to untargeted H I searches, targeting optically selected LSBGs in H I provides a means to obtain redshifts and test their UDG classification, as was done for SMuDGEs (Karunakaran et al. 2024). With the wealth of new H I surveys and facilities available in preparation for the SKA-Mid telescope, the opportunities to combine optical and H I data for understanding LSBGs and UDGs are expanding. For example, For et al. (2023) searched pre-pilot data from the Widefield ASKAP L-band Legacy All-sky Blind surveY (WALLABY) for detections of SMUDGES galaxies, finding one H I-rich LSBG and non-detections of H I in six putative UDGs.

In this work, we combine the optical and H I views of LSBGs and UDGs. The Early Science (ES) H I data from the MeerKAT International Giga Hertz Tiered Extragalactic Exploration MIGHTEE survey (Jarvis et al. 2016) provide a catalog of H I detections, and previous optical searches provide catalogs of LSBGs and UDG candidates; we introduce these catalogs in Section 2. We discuss how we cross-matched the catalogs in Section 3 and detail the new LSBGs and UDGs we identified from the H I detections in Section 4. In Section 5 we explore the H I content of optically identified galaxies. We discuss the implications of our results in Section 6 and end with our conclusions in Section 7.

2. Data

The field targeted by XMM-Large Scale Structure (XMM-LSS) survey is a well-studied extragalactic field that is contained within both HSC-SSP and MIGHTEE. For the purpose of this work, we focus on a subset of the region that contains the MIGHTEE ES footprint, shown in Figure 1.

2.1. MIGHTEE

2.1.1. H I data

The MIGHTEE ES data include three pointings in the XMM-LSS field. These pointings are referred to as XMM-LSS-12, XMM-LSS-13, and XMM-LSS-14 and are shown in Figure 1. The MIGHTEE ES data covers 1310–1420 MHz ($z = 0{-}0.084$) with a spectral resolution of 208.984 kHz (~44 km s^{-1} at $z = 0$). For logistical reasons, the bandwidth is split into three congruent spectral windows for processing. The typical noise is 81 μJy beam^{-1} in a single channel. Within a single channel, this corresponds to a 3σ column density sensitivity of 9.8×10^{19} atoms cm^{-2}.

The MIGHTEE ES H I source catalog was constructed via unguided visual inspection of the cubes to identify H I emission (Maddox et al. 2021). The H I masses were derived from measurements of the integrated flux density in moment-0 maps (Ponomareva et al. 2021; Rajohnson et al. 2022). The H I velocity widths at 50% of the peak flux density (W_{50}) were derived by fitting the busy function (Westmeier et al. 2014; Ponomareva et al. 2021). Distances for the MIGHTEE ES H I catalog are cosmological, with an assumed cosmology of $H_0 = 67.4\,{\rm km\,s^{-1}\,Mpc^{-1}}$, $\Omega_m = 0.315$, and $\Omega_\Lambda = 0.685$ (Planck Collaboration VI 2020). However, we adopt the distances based on local flow models for our analysis of LSBGs and UDGs, as described in Section 4.2. The 196 detections in the XMM-LSS ES region are shown in Figure 1.

2.1.2. Ancillary MIGHTEE data

The MIGHTEE fields were chosen specifically for their wealth of ancillary data, including deep optical photometry from HSC and deep near-infrared photometry from VISTA, as detailed in Maddox et al. (2021). In particular, the XMM-LSS field has either deep or ultra-deep HSC-SSP data in u, g, r, i, and z, which is ~0.5–1.5 mags deeper than the wide tier with the 5σ point-source detection limits for the deep (ultra-deep) data of $g = 27.5$ (28.1), $r = 27.1$ (27.7), and $i = 26.8$ (27.4) magnitudes Aihara et al. (2018).

The ancillary data were used to provide value-added information about the MIGHTEE H I detections. Elliptical apertures whose purpose was to encompass as much of the light as possible in the HSC g band image were applied to the photometric data from the u band to the NIR and used in the spectral energy distribution (SED) fitting to derive stellar masses and star formation rates (Maddox et al. 2021). Thus, we also have the size of the elliptical aperture used for photometry, the g and i band magnitudes, and the stellar masses for all MIGHTEE ES H I detections.

2.2. Optically selected LSBGs

We used the catalogs of G18 and L23 to select optically identified LSBGs within the MIGHTEE ES XMM-LSS footprint. Both works use the wide layer of the HSC-SSP, which covers five broad bands (g, r, i, z, y) with a depth of $g = 26.6$ mag, $r = 26.2$ mag, and $i = 26.2$ mag (5σ point-source detection) and a median seeing of 0.6″ (Aihara et al. 2018). The main difference between the two catalogs is that G18 used the internal data release S16A, while L23 used the public data release 2 (PDR2;

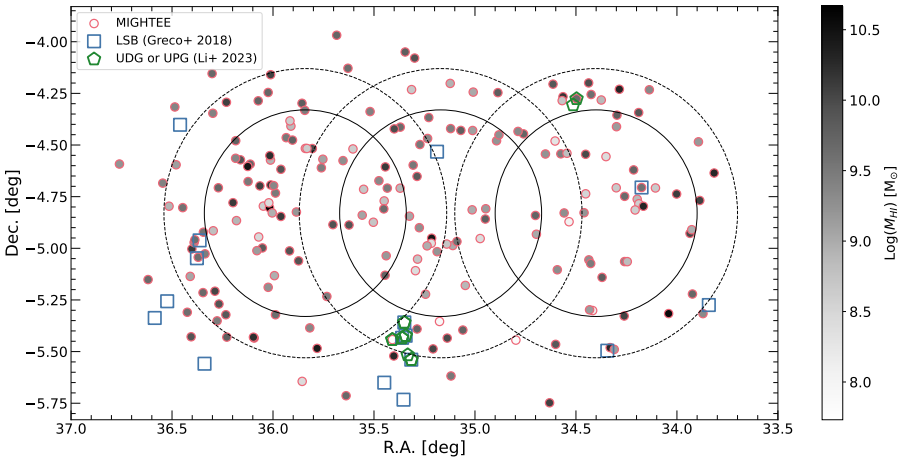

Fig. 1. Region of XMM-LSS covered in the MIGHTEE ES data. From left-to-right (decreasing right ascension), the three fields are XMM-LSS-14, XMM-LSS-13, and XMM-LSS-12. The solid lines indicate the full width half maximum of the MeerKAT primary beam, and the dashed lines represent the 30% response level. The MIGHTEE H I detections are shown as circles, shaded based on their H I mass. Also included are the LSBGs of G18 (blue squares) and the UDGs and UPGs of L23 (green pentagons) that fall within the considered footprint.

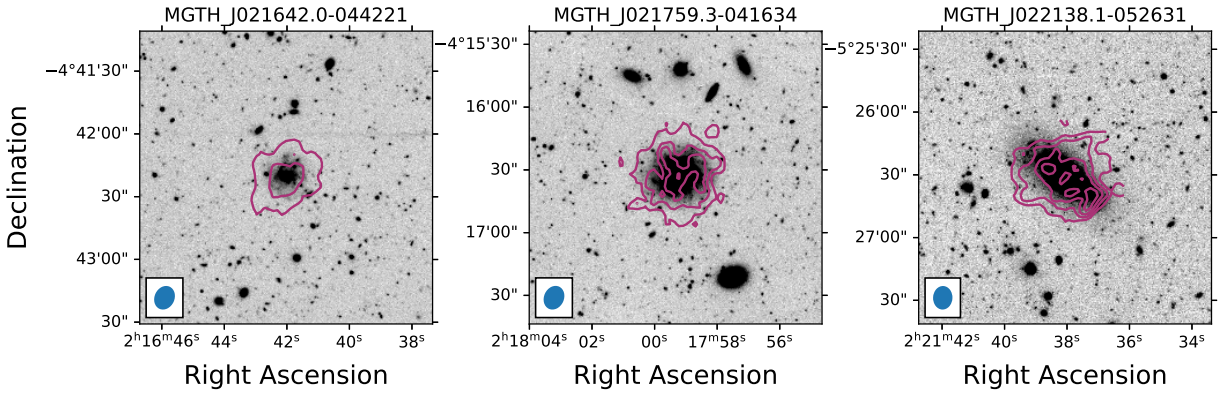

Fig. 2. The three cross-matched optical and H I sources. H I contours at $[2.5, 5, 7, 10] \times 10^{20}$ atoms cm^{-2} overlaid on g band images.

Table 1. H I and optical cross-matched sources.

Name MGTH_	Optical ID[a]	Sep. $''$	z_{HI}	z_{host}
J021642.0-044221	G267	0.6	0.042752	
J021759.3-041634	L25657	0.7	0.033398	0.035
J022138.1-052631	L86749	1.5	0.006912	0.032

Notes. [(a)]"G" refers to G18 and "L" to L23.

also known as S18A Aihara et al. 2019), which provides sky subtraction that is more appropriate for LSBGs.

Both works identified LSBGs, albeit in two different ways. In G18, masked galaxy cutouts were modeled as a two-dimensional point spread function (PSF)-convolved Sérsic function. Sources with $\overline{\mu}_{\rm eff,g} > 24.3$ and $2.5'' < r_{\rm eff} < 14''$ were identified as LSBGs, and they could be UDGs depending upon their (unknown) distance. In L23, a Spergel surface brightness profile (Spergel 2010; Tan et al. 2024) was convolved with the PSF to model the galaxies in the catalog. L23 also used a deblending technique that improved their completeness. The authors of L23 matched LSBGs to satellites of Milky Way-mass host galaxies from the NASA-Sloan Atlas[1], which provides compiled spectroscopic redshifts or direct distance measurements. They assigned the host redshift to the LSBG and then only provide catalogs for the galaxies that are either UDGs ($R_{eff} + \sigma(R_{eff}) > 1.5$ kpc and $\overline{\mu}_{\rm eff,g} + \sigma(\overline{\mu}_{\rm eff,g}) > 25.0$ mag arcsec^{-2} in their definition) or "ultra-puffy galaxies" (UPGs), galaxies that are outliers by more than 1.5σ from the mass-size relation defined by satellites of Milky Way analogs in the Local Volume (Carlsten et al. 2021). Thus, the L23 catalog has higher quality data with additional information (host redshift) but only for a subset of satellite galaxies compared to the G18 catalog. Given the different strengths of these two catalogs, we utilized both. Within the region of sky we considered (see Figure 1), there are 16 LSBGs from G18. The catalogs of L23 provide eight galaxies, five of which are classified as both UDG and UPG, two as UDGs only, and one as UPG only. Of the eight galaxies in L23, four are newly cataloged compared to G18. Given the improvements of L23 and additional information, we used measured properties from L23 over G18 when sources are cataloged in both. The galaxies from these catalogs are shown in Figure 1.

[1] https://nsatlas.org/

3. Cross-matching H I and optical

As a starting point, we cross-matched the existing MIGHTEE ES H I source list with the optically identified LSBGs of G18 and L23 with a $5''$ tolerance, finding three sources in common. These three sources are shown in Figure 2, where the MIGHTEE H I contours are plotted on (ultra-)deep g band HSC data. We list these sources in Table 1 along with their angular separation and both the MIGHTEE H I and host redshifts (if available).

The source MGTH_J021642.0-044221 is in G18 and thus had no existing redshift information available before. The source MGTH_J021759.3-041634 is in the UPG catalog of

L23 but not in the UDG catalog. The H I redshift is consistent with the assigned host galaxy redshift of 0.035. The source MGTH_J022138.1-052631 is in both the UPG and UDG catalogs of L23. However, the H I redshift (0.0069) is significantly lower than that of the assigned host (0.032), implying an incorrect host assignment. Thus this galaxy is much closer and has a much smaller physical effective radius than determined by L23. Based on the MIGHTEE redshift and cosmological distance, we find the physical effective radius (based on the L23 measured effective radius) is only 0.797 kpc, as opposed to the 3.594 kpc found by L23. Thus it would no longer be considered a UDG nor a UPG (for the updated stellar mass of $\log(M_*/M_\odot) = 6.7$).

4. H I-identified LSB galaxies

While there were not many direct cross-matches between the MIGHTEE H I detections and the optically identified LSBGs, H I is often an excellent tracer for finding LSBGs overlooked in the optical. Thus, we took the complementary approach of searching for LSBGs within the MIGHTEE H I detections.

4.1. Selecting potential LSBGs

To identify LSBGs, we performed surface brightness photometry of a subset of MIGHTEE H I detections. With 196 total detections in the XMM-LSS MIGHTEE ES field, we preselected the most promising LSB targets for surface brightness photometry following two different approaches.

The MIGHTEE ES XMM-LSS H I source list includes aperture photometry for all detections within the footprint of the deep or ultra-deep HSC data at the time of its creation (Maddox et al. 2021). There are five H I sources that fell outside the deep HSC coverage at this time, and they are not considered further in this work. In order to select targets for surface brightness photometry, we approximated the effective radius as one third of the total size of the aperture used for photometry[2] and used this to estimate $\overline{\mu}_{\rm eff,g}$. There were 19 sources with an estimated $\overline{\mu}_{\rm eff,g} > 24.3$, and we performed surface brightness photometry of these targets to accurately measure their $r_{\rm eff}$ and $\overline{\mu}_{\rm eff,g}$ in Section 4.2.

In addition, we undertook visual inspection of the g band fits images for all MIGHTEE XMM-LSS H I detections with (ultra-)deep HSC data to identify potential LSBGs for surface brightness photometry. This added an additional 14 targets, in addition to re-identifying seven of the automatically selected targets. One of the optically identified cross-matched galaxies (MGTH_J021759.3-041634) was missed by both of these approaches. It was the galaxy with the highest surface brightness of the cross-matched galaxies, and thus it is reasonable that it was the one that was missed in the target selection. For completeness, we added it to the list of galaxies for surface brightness photometry.

4.2. Surface brightness photometry

In total, there are 34 galaxies for which surface brightness photometry was performed. Ultra-deep data are preferred over deep data for photometry whenever available. The surface brightness photometry was done in two steps. In the first step, we conducted isophotal fitting on the i band image, with which we determined the geometry of the stellar disk, as detailed in Šiljeg et al. (2024). In the second step we extracted surface brightness profiles in g, r, and i bands following the procedure described in appendix A of Marasco et al. (2023) and fit these profiles with a Sérsic function to derive the surface brightness parameters. These steps are described briefly below.

The isophotal fitting step uses masked i band images smoothed with a Gaussian with a full width half maximum (FWHM) of 0.94″. A two-stage isophotal fitting was undertaken. The first stage was used to constrain the center of the galaxy, and in the second stage, the ellipticity and position angle were constrained. The final ellipticity and position angle values were taken as the median from the outer extents of the galaxies, at surface brightnesses between 24 and 27 mag arcsec^{-2}. Optical inclinations were derived with

$$\cos^2 i = \frac{(1-\epsilon)^2 - q_0^2}{1 - q_0^2}, \tag{1}$$

where ϵ denotes the ellipticity and q_0 is the intrinsic thickness of the stellar disk. We took $q_0 = 0.3$ as a common value for the dwarf irregular galaxies (e.g., Sánchez-Janssen et al. 2010) and applied it to almost all galaxies in the sample, except J022429.6-044037, for which the ellipticity was above 0.7 (hence giving an unphysical inclination). For this case, we set the inclination to $85_{-5}^{+4}{}^\circ$. The final geometric parameters of all galaxies are presented in Appendix A (Table A.1).

Using the derived geometric parameters, we created a set of ellipses of increasing semimajor axes with the same geometry and with widths equal to the FWHM of the PSF. In each ellipse, we took the mean value of the corresponding pixels in image units and corrected for inclination by multiplying with $\cos i$. The profile was extracted until $S/N = 1$ in a given ellipse. We converted image units (counts) to magnitudes using[3]:

$$m\,[\rm mag] = -2.5 \log_{10}(\Sigma\,\rm counts) + 27. \tag{2}$$

To characterize the obtained surface brightness profiles, we fit them with a Sérsic function. We independently fit profiles in all three bands ($X \in [g, r, i]$) for each galaxy, and we derived the following quantities: the central surface brightness ($\mu_{0,X}$), Sérsic index (n_X), effective radius ($r_{\rm eff,X}$), mean effective surface brightness ($\overline{\mu}_{\rm eff,X}$), and the apparent magnitude (m_X). Details on the fitting and error propagation are available in Šiljeg et al. (2024). The extracted profiles and the accompanying Sérsic fits are presented in Appendix A.

As some of the galaxies measured in this section are at very low redshift (with three galaxies below $z \lesssim 0.02$), we updated from using the cosmological distances based solely on redshift to using distances based on a flow model, where local motions of galaxies are taken into account when computing a distance from a velocity. We used Cosmic Flows 4 (Kourkchi et al. 2020; Valade et al. 2024) to determine the luminosity distances to all the sources. Errors on distances were obtained using the prescription from Haubner et al. (2025). We calculated the angular diameter distance from the luminosity distance as

$$D_A = D_L/(1+z)^2. \tag{3}$$

The various distances are collected in Table A.1, while the photometric values for each band are reported in Tables

[2] Elliptical apertures were individually set to contain all the light of each galaxy for the global photometry of the MIGHTEE H I ES catalog, as described in Section 2.1.2. For a typical Sérsic index of $n = 1$, the ratio of $r_{\rm eff}$ to the outermost radius (containing 95–99%) of the light is approximately three (Graham & Driver 2005).

[3] https://hsc-release.mtk.nao.ac.jp/doc/index.php/faq__pdr3

A.2, A.3 and A.4, along with Galactic extinction corrections from Schlafly & Finkbeiner (2011)[4] obtained through the NASA/IPAC Extragalactic Database (NED).

4.3. Newly identified LSBGs

Of the 34 galaxies for which we performed surface brightness photometry, 22 meet the LSBG requirements of G18 ($\overline{\mu}_{\rm eff,g} > 24.3$ and $r_{\rm eff,g} = 2.5-14''$). Of the 12 measured galaxies that did not meet the G18 criteria, one was too bright, two were too small and too bright, and nine were too small. These H I-identified LSBGs are listed in Table 2 with their key photometric values. Reassuringly, the three galaxies identified in the cross-match with G18 and L23 are identified as LSBs by this definition. Eleven of these sources were identified automatically, and eleven were only identified visually. Thus, both the automatic and visual classification were important for identifying LSBGs.

4.4. Newly identified UDGs

With the available distance information, we were able to additionally classify the galaxies as UDGs or not based on the definition $\overline{\mu}_{\rm eff,g} > 24\,{\rm mag\,arcsec^{-2}}$ and $R_{{\rm eff},g} > 1.5\,{\rm kpc}$ (van der Burg et al. 2016). In this case because we used the available distance information, we also applied the correction for cosmological dimming to derive the intrinsic effective surface brightness when classifying galaxies as UDGs. This correction excluded two galaxies, leaving us with 26 UDGs, seven of which are not classified as LSBGs due to having angular sizes smaller than 2.5″. These galaxies are also listed in Table 2. Of the three cross-matched galaxies, two are classified as UDGs. While the angular size of MGTH_J022138.1-052631 is found to be larger with the bespoke photometry of deeper HSC data, it is still not large enough to be classified as a UDG. Of the 26, 15 were identified in the automated approach and 11 only via visual inspection, again demonstrating the utility of both approaches.

5. H I content of optically identified LSBGs

While the optically identified LSBGs mostly fall in the outskirts of the MIGHTEE ES footprint and do not have direct H I detections, we can examine the known locations of the LSBGs in the MIGHTEE H I data cubes to search for marginal detections or to put an upper limit on their H I fluxes. Below we describe extraction of H I spectra at the known locations of the optical LSBGs and interpret the (non-)detections.

5.1. H I spectra

Before extracting H I spectra to search for marginal detections or place upper limits on non-detections, it was important to first consider where it is meaningful to extract data from in terms of the overall sensitivity of the data, i.e., the primary beam response. As can be seen in Figure 1, H I sources can be detected well beyond even the 30% primary beam response level. However, this depends on the intrinsic strength of the signal, and the data cubes themselves extend very far out in the primary beam response. To enforce some minimum quality on our flux estimates, we extracted the H I spectra only for sources within the 5% limit of the primary beam response. For each pointing there are three spectral windows that cover the full redshift range. We applied this requirement to each of these frequency cubes separately.

We applied the primary beam correction to the cubes before extracting the spectra. If a source was covered by more than one pointing, we combined the spectra using a linear weighting scheme based on the primary beam response. In all cases, we extracted the spectra using a 30″ aperture, which is consistent with expected H I source sizes[5]. Figure B.1 shows the extracted H I spectra for all detections in G18 and L23 that fell within 5% of the primary beam response in at least one spectral window.

The three cross-matched sources (G267, L25657, and L86749) are clearly seen in these spectra. G327 also has a detection, but this optical detection lies next to a dwarf galaxy merging with a massive galaxy (both gas rich). As seen in Figure 3, the aperture for the spectrum for G327 clearly falls on top of the H I emission for the larger galaxy in this system, MGTH_J021719.4-052851. With the poor spectral resolution of the early science data, it is not possible to distinguish whether there may be distinct H I emission arising from G327. We assumed the H I emission is fully from MGTH_J021719.4-052851 and used the rest of the spectrum for calculating an upper limit for G327.

No other sources have clear detections. A few sources have peaks around 4σ, but other sources have similar negative peaks. As a confirmation, we visually inspected the cubes for L5787, L45406, and G322. There was no evidence of emission for L45406 or G322. For L5787 (G315), there is emission at the frequency of the tentative detection (~1410 MHz); this is the very tip of the northern H I arm of NGC 895 (Namumba et al. 2023). Given the poor spectral resolution of the MIGHTEE H I ES data, it is not possible to say if there may be separate H I emission at this spatial and spectral location associated with L5787 or if it is a happen-chance alignment of a background source. With the full science data at full spectral resolution, it will be interesting to explore this feature to determine if L5787 may be a faint satellite of NGC 895 or a tidal feature. For now, we treat it as a non-detection. We report the standard deviations of the spectra in Table 3.

5.2. Gas content

Without a direct detection, we do not have a redshift and thus could not place direct limits on the H I mass, a distance-dependent quantity. However, the spectra can still be used to place upper limits on the integrated flux, and we can examine $M_{\rm HI}/M_*$, a distance-independent quantity[6].

We took the standard deviation of the spectra, assumed galaxies would occupy two channels ($88\,{\rm km\,s^{-1}}$ or $417.968\,{\rm kHz}$)[7], and calculated a 5σ upper limit for the integrated line flux, which is used to derive the upper limit for the H I mass. We applied the approach of L23 for calculating stellar masses, using the average of the $(g-r)$ and $(g-i)$

[4] The HSC employs a very similar photometric system (Kawanomoto et al. 2018) as the Sloan Digital Sky Survey (SDSS) (Fukugita et al. 1996).

[5] The three cross-matched sources in Section 3 have H I sizes of 28″–55″ based on the relation of Rajohnson et al. (2022).

[6] Note this is not strictly true as stellar masses require a k-correction that depends on redshift. However, for the redshift range considered here, this correction is small, and thus this statement is approximately true.

[7] The assumed width is important, as a narrower linewidth is easier to detect. We adopted two channels as a reasonable value for the range of galaxies we were focused on. The three cross-matched galaxies have W_{50} values of 46–99 $\rm km\,s^{-1}$, which are consistent with our assumed width.

Table 2. Surface brightness photometry of LSBGs and UDGs.

Name	$D_{L,CF}$ Mpc	$\bar{\mu}_{\rm eff,g}{}^{a}$ arcsec^{-2}	$e(\bar{\mu}_{\rm eff,g})$	$r_{\rm eff,g}$ $''$	$e(r_{\rm eff,g})$	$R_{\rm eff,g}$ kpc	$e(R_{\rm eff,g})$	$g-i^{a}$	$e(g-i)$	LSBG	UDG
MGTH_J021808.2-045217	104.0	25.71	0.01	2.56	0.07	1.23	0.13	0.40	0.00	yes	no
MGTH_J022138.1-052631	25.9	24.39	0.09	10.94	0.42	1.35	0.24	0.51	0.01	yes	no
MGTH_J022042.1-052115	30.1	24.45	0.04	5.02	0.28	0.72	0.13	0.59	0.03	yes	no
MGTH_J022051.9-045832	189.1	25.21	0.02	3.97	0.08	3.34	0.30	0.69	0.01	yes	yes
MGTH_J022429.6-044037	190.1	25.52	0.73	7.44	2.05	6.29	1.82	0.56	0.27	yes	yes
MGTH_J022400.9-044943	190.1	24.73	0.04	3.13	0.06	2.65	0.24	0.52	0.01	yes	yes
MGTH_J022358.3-050756	227.2	24.98	0.03	2.68	0.05	2.67	0.23	0.17	0.01	yes	yes
MGTH_J022357.0-051918	347.7	25.43	0.09	4.12	0.39	5.99	0.73	0.49	0.04	yes	yes
MGTH_J022350.6-045045	190.1	25.49	0.16	12.76	1.06	10.79	1.30	0.22	0.23	yes	yes
MGTH_J022332.2-044928	192.9	24.80	0.25	6.46	1.01	5.53	0.99	0.55	0.07	yes	yes
MGTH_J022117.8-045040	187.8	24.43	0.03	2.63	0.09	2.20	0.20	0.28	0.01	yes	yes
MGTH_J022443.4-045158	176.8	24.86	0.06	3.32	0.13	2.62	0.25	0.41	0.08	yes	yes
MGTH_J022045.0-050058	384.1	25.17	0.01	2.69	0.28	4.27	0.55	0.31	0.01	yes	yes
MGTH_J022522.7-045519	151.1	24.85	0.10	6.24	0.30	4.25	0.44	0.40	0.00	yes	yes
MGTH_J022026.3-045912	183.7	24.95	0.05	3.36	0.21	2.75	0.30	0.41	0.01	yes	yes
MGTH_J021848.1-045028	391.0	24.84	0.09	4.67	0.21	7.53	0.65	0.43	0.02	yes	yes
MGTH_J021818.0-043234	184.9	24.54	0.04	3.02	0.10	2.49	0.23	0.02	0.01	yes	yes
MGTH_J021759.3-041634	138.6	24.74	0.15	10.71	1.31	6.74	1.04	0.56	0.09	yes	yes
MGTH_J021724.3-043322	140.9	25.23	0.05	2.69	0.08	1.72	0.17	0.53	0.01	yes	yes
MGTH_J021645.4-042035	389.9	25.09	0.08	4.73	0.16	7.61	0.62	0.36	0.05	yes	yes
MGTH_J021642.0-044221	184.0	25.33	0.07	6.80	0.52	5.57	0.65	0.38	0.04	yes	yes
MGTH_J022029.4-041207	82.3	24.62	0.05	6.89	0.21	2.64	0.30	0.37	0.03	yes	yes
MGTH_J022056.9-045917	345.9	25.16	0.02	1.58	0.04	2.29	0.18	0.87	0.01	no	yes
MGTH_J022058.7-051320	291.4	24.58	0.03	1.43	0.05	1.78	0.15	0.87	0.02	no	yes
MGTH_J022110.7-050630	177.9	24.97	0.05	2.20	0.10	1.75	0.18	0.27	0.03	no	yes
MGTH_J022011.5-051047	225.9	25.22	0.01	1.96	0.03	1.94	0.16	0.41	0.01	no	yes
MGTH_J022338.7-042431	310.5	24.51	0.06	2.13	0.10	2.81	0.25	0.51	0.00	no	yes
MGTH_J021625.5-044228	183.9	24.32	0.04	2.20	0.10	1.80	0.18	0.38	0.01	no	yes
MGTH_J021534.4-042904	381.2	25.92	0.02	1.95	0.11	3.08	0.28	1.30	0.01	no	yes

Notes. $^{(a)}$Extinction-corrected.

mass-to-light ratios from Into & Portinari (2013), to the G18 galaxies.

The $M_{\rm HI}/M_*$ values are reported in Table 3. For the three cross-matches, these are measured values[8]. For all other sources, the values are 5σ upper limits. In general, the $M_{\rm HI}/M_*$ upper limits are quite high, so the lack of H I detections in these galaxies is not surprising. When examining Figure 1, it is clear that the optically identified LSBGs tend to lie at the edges of the ES footprint, where sensitivity is low. The full science data in XMM-LSS will include expanded spatial coverage with full sensitivity, so hopefully they will provide either detections or more constraining upper limits.

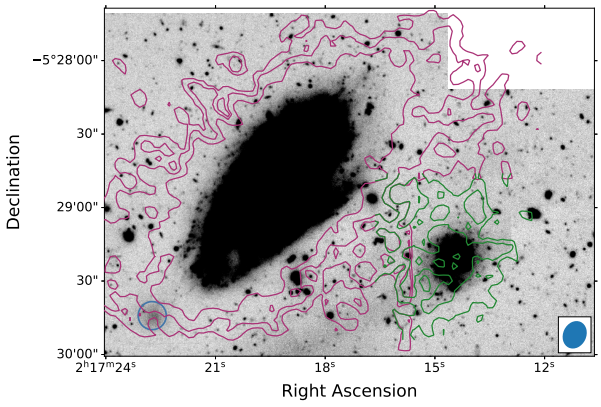

Fig. 3. Optically detected LSBG, G327 (blue circle), near two H I-detected galaxies. Red H I contours are MGTH_J021719.4-052851 and green contours are MGTH_J021714.5-052922. The levels are [2.5, 5, 10] $\times 10^{20}$ atoms cm^{-2} for both.

6. Discussion

6.1. Differences between photometry approaches

To compare the H I- and optically selected galaxies, it is important to understand the differences in the photometric approaches and the impact they might have. In the G18 catalog, the surface brightness distribution was modeled as a two-dimensional PSF-convolved Sérsic function in the i band. In the L23 catalog, the surface brightness distribution was modeled using a Spergel profile convolved with the PSF. In this work, one-dimensional surface brightness profiles sampled by the FWHM of the PSF were fit with a Sérsic function.

To assess the impact of the different photometric approaches, we compared the photometric properties of the three

[8] We note that we used the color-based mass-to-light stellar masses for consistency (see Section 6.1), but the cross-matched sources do have SED-based stellar masses available.

Table 3. H I properties of optically selected galaxies.

Name	RA	Dec	z_{host}	z_{min}	z_{max}	rms mJy	M_{HI}/M_*
G262	36.46018	−4.4021		0.0011	0.084	0.66	<18.10
G265	36.37673	−5.04815		0.0011	0.084	0.25	<8.36
G266	36.3633	−4.96164		0.0011	0.084	0.22	<5.47
G267	34.17509	−4.70562		0.0011	0.084	0.11	9.51
G268	35.18785	−4.53235		0.0011	0.084	0.13	<1.50
G304	36.52391	−5.25631		0.0011	0.084	0.82	<19.18
G308	36.58562	−5.33722		0.0293	0.084	1.64	<13.41
G309	36.33909	−5.5587		0.0293	0.084	1.43	<41.79
G318	35.35374	−5.73281		0.068	0.084	2.09	<6.56
G319	35.44907	−5.65036		0.0011	0.084	1.17	<9.11
G322	33.84203	−5.27461		0.0011	0.084	0.58	<10.97
G327	34.34471	−5.49559		0.0011	0.084	0.35	<7.73
L21295	35.343	−5.423	0.032	0.0011	0.084	0.33	<5.54
L25657	34.497	−4.276	0.035	0.0011	0.084	0.26	3.52
L30385	35.333	−5.516	0.032	0.0011	0.084	0.49	<23.22
L35220	34.514	−4.306	0.034	0.0011	0.084	0.24	<30.57
L45406	35.35	−5.359	0.032	0.0011	0.084	0.25	<20.19
L55931	35.315	−5.539	0.032	0.0011	0.084	0.53	<5.49
L5787	35.361	−5.434	0.032	0.0011	0.084	0.36	<34.81
L86749	35.409	−5.442	0.032	0.0011	0.084	0.47	9.72

Table 4. Comparison of photometric measurements.

Names	Property[a]	This work	G18/L23
J021642.0-044221/ G267	$g-i$	0.42 ± 0.04	0.43 ± 0.24
	m_i	18.85 ± 0.03	18.89 ± 0.24
	r_{eff} ($''$)[b]	6.44 ± 0.42	6.27 ± 0.79
	$\overline{\mu}_{eff,g}$[c]	25.18 ± 0.25	25.30 ± 0.24
J021759.3-041634/ L25657	$g-i$	0.59 ± 0.09	0.66 ± 0.05
	m_i	17.07 ± 0.04	17.02 ± 0.07
	r_{eff} ($''$)[b]	10.21 ± 0.76	8.52 ± 0.35
	$\overline{\mu}_{eff,g}$[c]	24.66 ± 0.18	24.33 ± 0.05
J022138.1-052631/ L86749	$g-i$	0.54 ± 0.01	0.43 ± 0.05
	m_i	16.73 ± 0.01	18.99 ± 0.08
	r_{eff} ($''$)[b]	11.17 ± 0.48	5.37 ± 0.31
	$\overline{\mu}_{eff,g}$[c]	24.24 ± 0.15	25.06 ± 0.06

Notes. [a]Not corrected for extinction. [b]Measured in the i band. [c]$\overline{\mu}_{eff,g} = m_g + 2.5 \log_{10}(2\pi r_{eff}^2)$.

cross-matched galaxies in Table 4. While there are only three sources, we observed that two of them are generally consistent between the different approaches to surface brightness photometry. The third source is measured to be much brighter and more extended in this work. This source is also the galaxy that had an erroneous host assignment in L23. Visual inspection of the images did not reveal an obvious explanation for the difference in extent (and total magnitude), but it showed that our photometry encompasses the full source extent.

Furthermore, as the aperture magnitudes from the MIGHTEE ES catalog were used for the SED-based stellar masses, ensuring the consistency of the aperture magnitudes with our derived photometry allows us to use the stellar masses in the MIGHTEE ES catalog. Figure 4 presents a comparison of the two sets of photometry, showing that the two approaches result in consistent measurements of the total magnitude. However, when comparing the SED-based stellar masses to those derived using mass-to-light (ML) ratios (as for L23), we found a systematic offset with the ML-based stellar masses that is ∼0.3 dex higher than the SED-based stellar masses. The SED-based stellar masses are generally considered more robust, while the ML-based stellar masses require less observational data. The systematic offset that we found is indicative of the underlying systematics present in stellar mass estimates of all types. Given this, we always explicitly state what stellar mass estimates we use throughout the rest of this section.

6.2. HI versus optically identified populations

The optically and H I identified LSBGs and UDGs in this work are mostly distinct populations, with only three galaxies in common. Here we explore their properties to better understand the differences between the two populations. Throughout this section, for the three galaxies detected in both H I and optical searches, we plot them with their properties as measured in this work and the original optical measurements from either L23 or G18. We highlight these three galaxies so it is clear that they are the common galaxies.

Figure 5 shows a comparison of the gas fraction and color ($g-i$) of the MIGHTEE-detected LSBGs and UDGs of this work in relation to the LSBGs of G18 and the UDGs and UPGs of L23. In this case, we used stellar masses based on the same ML ratio for both samples to enable the closest comparison. The H I-detected galaxies of this work are predominantly blue, as expected for H I-selected galaxies. Some of the optically identified galaxies exhibit similar blue colors, and thus it may be initially surprising that not more of the optically identified galaxies were detected in the MIGHTEE H I data. However, the upper limits on the H I content of the optically identified galaxies are not very constraining, with upper limits on M_{HI}/M_* ranging from ∼5−34. Thus, the bluer optically identified galaxies may still host significant amounts of H I. It is also worth noting the large

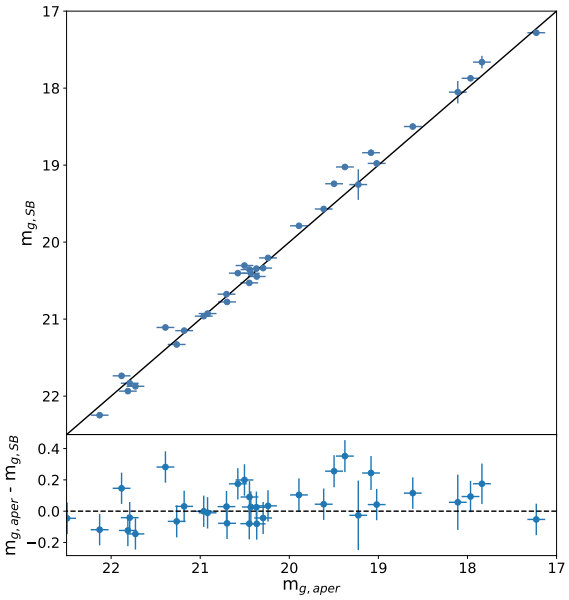

Fig. 4. Comparison of apparent (non-extinction corrected) g band magnitudes derived through aperture and surface brightness photometry. *Upper:* Magnitudes derived through surface brightness photometry (y-axis) plotted against those derived from aperture photometry (x-axis). *Lower:* Differences between the two magnitudes plotted against the apparenet magnitude from aperture photometry.

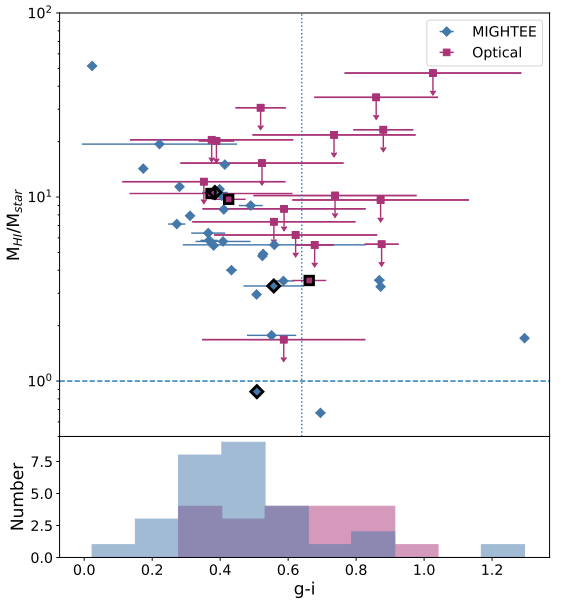

Fig. 5. Colors of the optically and H I-selected galaxies. *Upper:* $g - i$ color vs. $M_{\rm HI}/M_*$. Downward arrows indicate upper limits. Symbols highlighted in black indicate the cross-matched galaxies that are plotted twice. The vertical dotted line at 0.64 indicates the cut between "red" and "blue" used in G18. The dashed horizontal line indicates a $M_{\rm HI}/M_*$ value of one. *Lower:* Histogram of the color distribution of both the MIGHTEE-detected (blue) and optically detected galaxies (pink).

gas fractions of the LSBGs that do have H I detections – only two galaxies in total have more mass in stars than H I.

Given the non-stringent H I gas fraction limits, it is understandable why the optically identified blue LSBGs are not detected in MIGHTEE. More puzzling is that the MIGHTEE-detected LSBGs and UDGs are not identified in the optical searches. For L23, this may be partially explained by the requirement of a host galaxy for an associated redshift, as the H I-selected population from MIGHTEE may not have the host galaxies required by L23. In addition, L23 used a fainter effective surface brightness cut for their definition of a UDG that would exclude some of the UDGs in our definition. For comparison to G18, we looked at the two essential metrics, $r_{\rm eff}$ and $\overline{\mu}_{\rm eff,g}$, as seen in Figure 6. The MIGHTEE UDGs that are not also LSBGs would be excluded from G18 due to their angular size being smaller than the minimum used in their selection. Additionally, it is possible that the automated source finding and characterization of G18 and L23 would result in larger sources being shredded if the emission was patchy, as is often the case for H I-rich galaxies. Overall, there is not one clear reason that the MIGHTEE LSBGs were missed in the optical searches, but it highlights the utility of targeted photometry based on H I detections for identifying LSBGs.

6.3. Impacts of survey footprint and redshift limits

As discussed above, very few of the optically identified LSBGs are detected in the MIGHTEE ES data. This can be mostly explained by the footprint of the MIGHTEE ES data. As seen in Figure 1, most of the optical detections fall in the outskirts of the ES data, with all except two beyond the 50% response level and almost half beyond the 30% response level. However, it is also worth considering the impact of redshift limits, as the detection of H I requires that the galaxy has a redshift that falls within the frequency coverage of the observation. As seen in Table 3, the redshifts of the associated hosts for the galaxies from L23 all fall within the limits of the MIGHTEE ES data ($z = 0{-}0.084$); thus these would be detected if the observations were sensitive enough, assuming the host associations are accurate. The galaxies from G18 do not have redshifts available; however, Greene et al. (2022) used a statistical approach to estimate that ~50% of the galaxies are at $z < 0.05$, with essentially no galaxies beyond $z = 0.15$. The MIGHTEE redshift limits extend to $z = 0.084$, and thus we might reasonably expect the majority of G18 galaxies to fall within the observed frequency range and to be detected if there were sufficient sensitivity.

6.4. The baryonic Tully-Fisher relation

The baryonic Tully-Fisher relation (bTFr) relates total baryonic mass to the rotational velocity of a galaxy. It is one of the tightest scaling relations known, with extremely low intrinsic scatter (e.g., Lelli et al. 2016; Papastergis et al. 2016; Ponomareva et al. 2018; Lelli et al. 2019). Recently, some gas-rich UDGs have been proposed to be outliers to this relation (e.g., Mancera Piña et al. 2019b, 2020; Hu et al. 2023; Šiljeg et al. 2024) due to having lower rotation velocities than expected for their baryonic mass, potentially revealing new insights into galaxy formation (e.g., Mancera Piña et al. 2020, 2024; Afruni et al. 2025). Ponomareva et al. (2021) studied the bTFr for all MIGHTEE ES galaxies where robust kinematic models could be derived. Figure 7 shows the bTFr using the outermost rotational velocity, $V_{\rm out}$, from Ponomareva et al. (2021), and the LSBGs and UDGs identified in this work are highlighted. There are only four galaxies from this work that have the kinematic information required to be shown in this plot, and all four are classified as both UDG and LSBG. Three of these galaxies are fully consistent with this relation, while one is potentially an outlier. Interestingly, this potential outlier

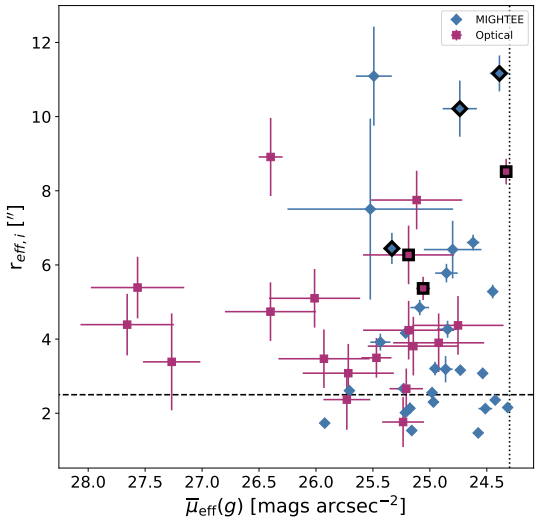

Fig. 6. $\overline{\mu}_{\rm eff,g}$ color vs. $r_{\rm eff}$. Symbols highlighted in black indicate galaxies that are identified by both MIGHTEE and the works of G18 and L23, and they are plotted twice (once for each measurement). The vertical dotted line and dashed horizontal lines indicate the LSBG cuts of G18 for surface brightness and effective radius.

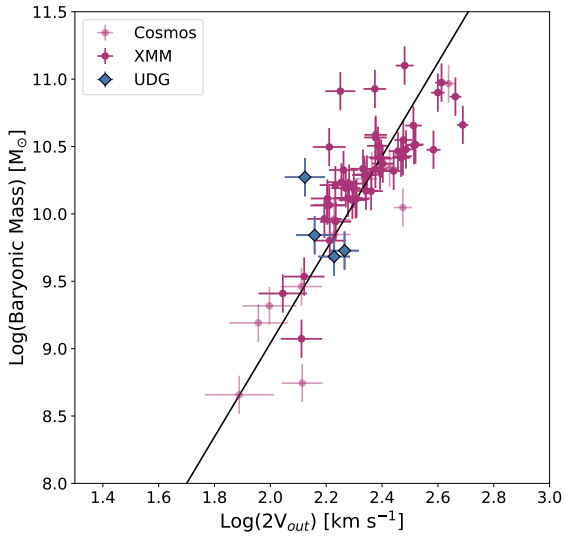

Fig. 7. Baryonic mass vs. outermost rotational velocity. MIGHTEE galaxies are shown with magenta circles, with galaxies from the COSMOS field (not searched for LSBG/UDGs) in a lighter magenta. The four galaxies of this work (meeting both LSBG and UDG classification criteria) are shown as blue diamonds. The derived bTFr from Ponomareva et al. (2021) is shown by the black line.

(J022350.6-045045) has one of the largest physical sizes, with an effective radius of 10.79 kpc, although such a large size could be indicative of disruption or non-equilibrium (e.g., Mihos et al. 2015; Venhola et al. 2017). However, there are other galaxies in the XMM-LSS field that were not identified in this work as an LSBG or UDG that show similar offsets from the bTFr. The relatively poor spectral resolution of the early science data naturally biases us toward sources that are spectrally wide and hence more likely to have higher rotational velocities for a given inclination. This limits the exploration of UDGs that might be offset from the bTFr toward lower rotational velocities. Deriving updated and additional rotation velocities with the MIGHTEE full science data at the full velocity resolution will help reveal how the UDG and LSBG populations as a whole connect to the bTFr.

6.5. LSBGs in an H I-identified population

The LSBGs and UDGs we identified here appear to be very gas rich, as seen in Figure 5. We examined this further with Figure 8, looking at $M_{\rm HI}$ versus M_* for all MIGHTEE detections in XMM-LSS and using the SED-based stellar masses derived in a consistent manner for all MIGHTEE detections. The LSBGs and UDGs are clearly more gas rich than the full MIGHTEE sample (Maddox et al. 2021). Thus, for a given stellar mass, lower surface brightness galaxies tend to have more mass in H I than those with a higher surface brightness. As seen in the previous section, there seems to be no trend with surface brightness in our sample for galaxies to lie on or fall off the bTFr (for the subset with adequate kinematics in the ES data). This implies that for a given rotation velocity (or dark matter halo mass), galaxies of different surface brightnesses have similar baryonic masses. Thus, the more gas-rich nature of the LSBGs and UDGs indicates that they have not turned their gas into stars as efficiently, in agreement with the arguments put forth by Kado-Fong et al. (2022).

It is also worthwhile to briefly compare the UDGs and LSBGs of this work to other H I-selected samples. Leisman et al. (2017) provided the first catalog of H I-selected UDGs from the ALFALFA H I survey, with their broad sample having $\overline{\mu}_{\rm eff,r} > 24$ mag arcsec^{-2}. They found that the H I-selected UDGs were gas rich compared to the general ALFALFA population, akin to how we find that our UDGs and LSBGs are gas rich compared to other MIGHTEE detections. As MIGHTEE H I detections have a similar $M_{\rm HI}$ and M_* compared to ALFALFA (Maddox et al. 2021), our UDGs and LSBGs are gas rich in comparison to that larger reference population as well, as can also be seen in Figure 8. More recently, O'Beirne et al. (2025) identified LSBGs in the WALLABY pilot survey data. Their sample appears to have a similar behavior for $M_{\rm HI}$-M_* when compared to ALFALFA (see their figure 5). However, they used a less stringent requirement of $\overline{\mu}_{\rm eff,g} > 23$ mag arcsec^{-2} for their definition of LSBGs. Thus, it could be that it is only at a lower surface brightnesses (e.g., $\gtrsim$24 mag arcsec^{-2}) that there is a distinction in the H I mass versus stellar mass for galaxies. Exploring gas-richness in different regimes of surface brightness is an interesting avenue for future exploration.

7. Conclusions

In this work, we have used the MIGHTEE early science H I data in the XMM-LSS field to understand the LSBG population, including UDGs. This was done by searching for new LSBGs missed in the previous optical searches and studying the gas content of all known LSBGs within the footprint.

Cross-matching of the H I detections and optically identified LSBGs from G18 and L23 revealed three sources in common. The MIGHTEE H I detection provides direct redshifts for these galaxies. One redshift is completely new, and a previous redshift assignment is updated.

Thirty-four MIGHTEE galaxies were chosen as potential LSBG candidates. Dedicated surface brightness photometry revealed that 29 met either the LSBG definition of G18 ($\overline{\mu}_{\rm eff,g} > 24.3$ mag arcsec^{-2} and $2.5'' < r_{\rm eff} < 14''$; 22 galaxies) and/or the adopted UDG definition ($\overline{\mu}_{\rm eff,g} > 24$ mag arcsec^{-2} and $R_{{\rm eff},g} >$

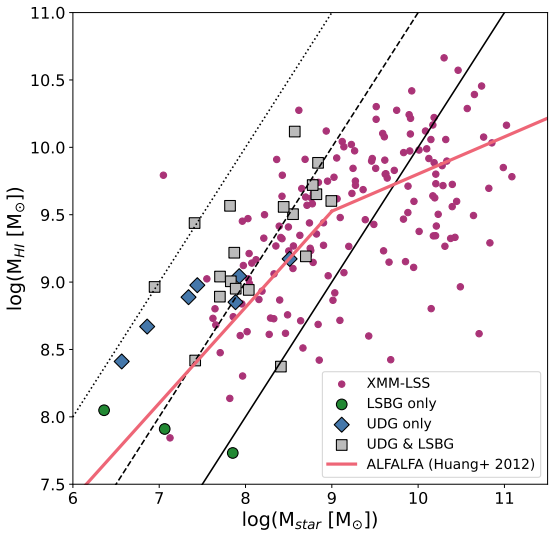

Fig. 8. $M_{\rm HI}$ vs. M_* for all MIGHTEE galaxies in XMM-LSS. The UDGs and LSBGs are indicated, and the diagonal solid, dashed, and dotted lines indicate $M_{\rm HI}$ to M_* ratios of 1, 10, and 100. All stellar masses are derived from SED estimates. Galaxies from this work that meet only the LSBG definition (green circles), UDG definition (blue diamonds), or both (gray squares) are indicated separately. The solid red line indicates the relation from the ALFALFA survey (Huang et al. 2012).

1.5 kpc; 26 galaxies). Furthermore, 20 optically identified galaxies from G18 and L23 fell within the bounds of the MIGHTEE ES footprint (i.e., within 5% of the primary beam response of at least one field). We performed a targeted search for H I emission at the locations of these optically selected galaxies but identified no new H I emission beyond the three cross-matched sources. The upper limits on the gas fractions for these galaxies are not constraining, as the optically identified galaxies fall mostly on the edges of the MIGHTEE ES footprint, with reduced sensitivity.

Comparison between the H I- and optically selected samples showed that H I-detected galaxies tend toward bluer colors on average, but in general the H I-selected sample overlaps with the optically selected sample in color, surface brightness, and size. The lack of identification of the H I-selected galaxies in the optical catalogs is likely due to a combination of different selection cuts in the optical catalogs (e.g., minimum sizes and requiring host galaxies) combined with a targeted surface brightness photometry approach for patchy LSB sources instead of automated source detection and modeling.

The LSBGs and UDGs of MIGHTEE were examined and compared to the full MIGHTEE population. Only four have available kinematics from Ponomareva et al. (2021), three of which show no clear offset of the full population from the baryonic Tully-Fisher relation. Our analysis, however, is biased toward galaxies with larger rotational velocities due to the poor spectral resolution of the data. Further studies with more LSBGs and careful derivation of the kinematics are therefore warranted. This will be especially important when the MIGHTEE data at full spectral resolution are available in this region. The MIGHTEE LSBGs are also clearly gas rich compared to the full population of MIGHTEE detections, pointing to a scenario where their LSB nature arises from not efficiently converting gas to stars. A comparison to other H I samples, namely ALFALFA (Leisman et al. 2017) and WALLABY (O'Beirne et al. 2025), indicated that a surface brightnesses lower than ~24 mag arcsec^{-2} may be where gas fractions start to significantly change.

The optical and H I identification both play important roles in identifying LSBGs. Here we have shown samples from the same footprint, where LSBGs identified via their stellar versus gaseous content are similar in number but with very little overlap, showing the utility of using both tracers to understand the full population. As both optical and H I surveys increase in depth, we may expect the overlap to grow between the two tracers but for both to always have valuable roles to play: optical for identifying gas-poor LSBGs and H I for identifying "too shy to shine" galaxies that have minimal stellar components.

Acknowledgements. We thank the anonymous referee for their helpful comments, and J. M. van der Hulst for insightful discussion. PEMP is funded by the Dutch Research Council (NWO) through the Veni grant VI.Veni.222.364. MB gratefully acknowledges financial support from the Flemish Fund for Scientific Research (FWO-Vlaanderen) and the South African National Research Foundation (NRF) under their Bilateral Scientific Cooperation program (grant G0G0420N), and from the Belgian Science Policy Office (BELSPO), under grant BL/02/SA12 (GALSIMAS). MJJ acknowledges the support of the STFC consolidated grant [ST/S000488/1] and [ST/W000903/1], a UKRI Frontiers and the Hintze Family Charitable Foundation through the Oxford Hintze Centre for Astrophysical Surveys. GS acknowledge funding from IRMIA++, SARAO (Grant no.: 97882), and the European Union's Horizon 2020 research and innovation programme under the Marie Skłodowska-Curie grant agreement No 101147719. The MeerKAT telescope is operated by the South African Radio Astronomy Observatory, which is a facility of the National Research Foundation, an agency of the Department of Science, Technology and Innovation. We acknowledge the use of the ilifu cloud computing facility – www.ilifu.ac.za, a partnership between the University of Cape Town, the University of the Western Cape, Stellenbosch University, Sol Plaatje University and the Cape Peninsula University of Technology. The ilifu facility is supported by contributions from the Inter-University Institute for Data Intensive Astronomy (IDIA – a partnership between the University of Cape Town, the University of Pretoria and the University of the Western Cape), the Computational Biology division at UCT and the Data Intensive Research Initiative of South Africa (DIRISA). This work made use of the CARTA (Cube Analysis and Rendering Tool for Astronomy) software (DOI 10.5281/zenodo.3377984 – https://cartavis.github.io). The Hyper Suprime-Cam (HSC) collaboration includes the astronomical communities of Japan and Taiwan, and Princeton University. The HSC instrumentation and software were developed by the National Astronomical Observatory of Japan (NAOJ), the Kavli Institute for the Physics and Mathematics of the Universe (Kavli IPMU), the University of Tokyo, the High Energy Accelerator Research Organization (KEK), the Academia Sinica Institute for Astronomy and Astrophysics in Taiwan (ASIAA), and Princeton University. Funding was contributed by the FIRST program from Japanese Cabinet Office, the Ministry of Education, Culture, Sports, Science and Technology (MEXT), the Japan Society for the Promotion of Science (JSPS), Japan Science and Technology Agency (JST), the Toray Science Foundation, NAOJ, Kavli IPMU, KEK, ASIAA, and Princeton University. This work made use of Astropy (http://www.astropy.org) a community-developed core Python package and an ecosystem of tools and resources for astronomy (Astropy Collaboration 2013, 2018, 2022).

References

Afruni, A., Marinacci, F., Mancera Piña, P. E., & Fraternali, F. 2025, MNRAS, 538, 60
Aihara, H., Arimoto, N., Armstrong, R., et al. 2018, PASJ, 70, S4
Aihara, H., AlSayyad, Y., Ando, M., et al. 2019, PASJ, 71, 114
Amorisco, N. C., & Loeb, A. 2016, MNRAS, 459, L51
Astropy Collaboration (Robitaille, T. P., et al.) 2013, A&A, 558, A33
Astropy Collaboration (Price-Whelan, A. M., et al.) 2018, AJ, 156, 123
Astropy Collaboration (Price-Whelan, A. M., et al.) 2022, ApJ, 935, 167
Carlsten, S. G., Beaton, R. L., Greco, J. P., & Greene, J. E. 2019, ApJ, 879, 13
Carlsten, S. G., Greene, J. E., Greco, J. P., Beaton, R. L., & Kado-Fong, E. 2021, ApJ, 922, 267
Conselice, C. J. 2018, Res. Notes Am. Astron. Soc., 2, 43
Dalcanton, J. J., Spergel, D. N., & Summers, F. J. 1997, ApJ, 482, 659
Di Cintio, A., Brook, C. B., Dutton, A. A., et al. 2017, MNRAS, 466, L1
For, B. Q., Spekkens, K., Staveley-Smith, L., et al. 2023, MNRAS, 526, 3130
Fukugita, M., Ichikawa, T., Gunn, J. E., et al. 1996, AJ, 111, 1748
Graham, A. W., & Driver, S. P. 2005, PASA, 22, 118

Greco, J. P., Greene, J. E., Strauss, M. A., et al. 2018, ApJ, 857, 104
Greene, J. E., Greco, J. P., Goulding, A. D., et al. 2022, ApJ, 933, 150
Haubner, K., Lelli, F., Di Teodoro, E., et al. 2025, A&A, 696, A185
Hu, H.-J., Guo, Q., Zheng, Z., et al. 2023, ApJ, 947, L9
Huang, S., Haynes, M. P., Giovanelli, R., & Brinchmann, J. 2012, ApJ, 756, 113
Impey, C., Bothun, G., & Malin, D. 1988, ApJ, 330, 634
Into, T., & Portinari, L. 2013, MNRAS, 430, 2715
Janowiecki, S., Jones, M. G., Leisman, L., & Webb, A. 2019, MNRAS, 490, 566
Jarvis, M., Taylor, R., Agudo, I., et al. 2016, in MeerKAT Science: On the Pathway to the SKA, 6
Kado-Fong, E., Greene, J. E., Huang, S., & Goulding, A. 2022, ApJ, 941, 11
Karunakaran, A., Motiwala, K., Spekkens, K., et al. 2024, ApJ, 975, 91
Kawanomoto, S., Uraguchi, F., Komiyama, Y., et al. 2018, PASJ, 70, 66
Koda, J., Yagi, M., Yamanoi, H., & Komiyama, Y. 2015, ApJ, 807, L2
Kourkchi, E., Courtois, H. M., Graziani, R., et al. 2020, AJ, 159, 67
Leisman, L., Haynes, M. P., Janowiecki, S., et al. 2017, ApJ, 842, 133
Lelli, F., McGaugh, S. S., & Schombert, J. M. 2016, ApJ, 816, L14
Lelli, F., McGaugh, S. S., Schombert, J. M., Desmond, H., & Katz, H. 2019, MNRAS, 484, 3267
Li, J., Greene, J. E., Greco, J. P., et al. 2023, ApJ, 955, 1
Maddox, N., Frank, B. S., Ponomareva, A. A., et al. 2021, A&A, 646, A35
Mancera Piña, P. E., Aguerri, J. A. L., Peletier, R. F., et al. 2019a, MNRAS, 485, 1036
Mancera Piña, P. E., Fraternali, F., Adams, E. A. K., et al. 2019b, ApJ, 883, L33
Mancera Piña, P. E., Fraternali, F., Oman, K. A., et al. 2020, MNRAS, 495, 3636
Mancera Piña, P. E., Golini, G., Trujillo, I., & Montes, M. 2024, A&A, 689, A344
Marasco, A., Belfiore, F., Cresci, G., et al. 2023, A&A, 670, A92
Mihos, J. C., Durrell, P. R., Ferrarese, L., et al. 2015, ApJ, 809, L21
Namumba, B., Román, J., Falcón-Barroso, J., et al. 2023, MNRAS, 521, 5177
O'Beirne, T., Staveley-Smith, L., Kilborn, V. A., et al. 2025, PASA, 42, e087
Papastergis, E., Adams, E. A. K., & van der Hulst, J. M. 2016, A&A, 593, A39
Planck Collaboration VI. 2020, A&A, 641, A6
Ponomareva, A. A., Verheijen, M. A. W., Papastergis, E., Bosma, A., & Peletier, R. F. 2018, MNRAS, 474, 4366
Ponomareva, A. A., Mulaudzi, W., Maddox, N., et al. 2021, MNRAS, 508, 1195
Posti, L., Pezzulli, G., Fraternali, F., & Di Teodoro, E. M. 2018, MNRAS, 475, 232
Rajohnson, S. H. A., Frank, B. S., Ponomareva, A. A., et al. 2022, MNRAS, 512, 2697
Román, J., Beasley, M. A., Ruiz-Lara, T., & Valls-Gabaud, D. 2019, MNRAS, 486, 823
Rong, Y., Guo, Q., Gao, L., et al. 2017, MNRAS, 470, 4231
Sánchez-Janssen, R., Méndez-Abreu, J., & Aguerri, J. A. L. 2010, MNRAS, 406, L65
Sandage, A., & Binggeli, B. 1984, AJ, 89, 919
Schlafly, E. F., & Finkbeiner, D. P. 2011, ApJ, 737, 103
Šiljeg, B., Adams, E. A. K., Fraternali, F., et al. 2024, A&A, 692, A217
Silk, J. 2019, MNRAS, 488, L24
Spergel, D. N. 2010, ApJS, 191, 58
Tan, Q.-H., Daddi, E., de Souza Magalhães, V., et al. 2024, A&A, 684, A23
Valade, A., Libeskind, N. I., Pomarède, D., et al. 2024, Nat. Astron., 8, 1610
van der Burg, R. F. J., Muzzin, A., & Hoekstra, H. 2016, A&A, 590, A20
van Dokkum, P. G., Abraham, R., Merritt, A., et al. 2015, ApJ, 798, L45
Venhola, A., Peletier, R., Laurikainen, E., et al. 2017, A&A, 608, A142
Watkins, A. E., Salo, H., Kaviraj, S., et al. 2023, MNRAS, 521, 2012
Westmeier, T., Jurek, R., Obreschkow, D., Koribalski, B. S., & Staveley-Smith, L. 2014, MNRAS, 438, 1176
Wright, A. C., Tremmel, M., Brooks, A. M., et al. 2021, MNRAS, 502, 5370
Yagi, M., Koda, J., Komiyama, Y., & Yamanoi, H. 2016, ApJS, 225, 11
Yozin, C., & Bekki, K. 2015, MNRAS, 452, 937
Zaritsky, D., Donnerstein, R., Karunakaran, A., et al. 2022, ApJS, 261, 11
Zaritsky, D., Donnerstein, R., Dey, A., et al. 2023, ApJS, 267, 27

Appendix A: Surface brightness photometry

This appendix presents the surface brightness photometry values for all galaxies that were measured. Table A.1 presents the global values for all galaxies, including their name, the depth of the data, the various distances to the galaxy, and the global optical morphology, and Tables A.2, A.3 and A.4 present the photometry for the g, r and i bands, not corrected for Galactic extinction. In addition, we show the surface brightness profiles and Sérsic profile fits from which all these properties were derived in Figure A.1.

Table A.1. Global properties of all galaxies with surface brightness photometry.

Name MGTH_	Data	z	$D_{L,z}$[a] Mpc	$D_{L,CF}$[b]	e($D_{L,CF}$)	$D_{AD,CF}$[c]	i °	e(i) °	PA °	e(PA) °
J021534.4-042904	Ultra	0.082098	350.2	381.2	28.5	325.6	72	2	19.4	0.8
J021625.5-044228	Ultra	0.042752	186.1	183.9	16.1	169.2	29	11	-134.2	29.2
J021642.0-044221	Ultra	0.042752	186.1	184.0	16.1	169.2	41	10	-58.4	21.4
J021645.4-042035	Ultra	0.083651	356.6	389.9	29.0	332.0	54	11	-9.9	30.6
J021714.5-052922	Ultra	0.017464	77.0	69.5	8.2	67.1	32	8	-33.4	48.4
J021724.3-043322	Ultra	0.034075	149.0	140.9	13.3	131.8	56	5	-17.7	3.9
J021759.3-041634	Ultra	0.033398	146.1	138.6	13.1	129.8	45	8	-76.0	15.6
J021808.2-045217	Ultra	0.025756	113.1	104.0	10.7	98.8	55	3	1.9	3.9
J021818.0-043234	Ultra	0.042912	186.8	184.9	16.2	170.0	62	5	12.7	4.5
J021848.1-045028	Ultra	0.083866	357.4	391.0	29.0	332.9	50	14	77.8	28.1
J021934.4-042846	Ultra	0.069497	298.4	315.2	24.4	275.5	46	2	-44.6	0.8
J022011.5-051047	Ultra	0.05195	225.1	225.9	18.8	204.1	40	3	55.8	5.9
J022026.3-045912	Deep	0.042591	185.4	183.7	16.1	169.0	51	6	-87.0	3.5
J022029.4-041207	Ultra	0.020365	89.7	82.3	9.1	79.0	66	2	-46.5	8.2
J022042.1-052115	Deep	0.007359	32.6	30.1	4.9	29.6	46	8	-69.3	4.0
J022045.0-050058	Ultra	0.082615	352.3	384.1	28.6	327.7	27	4	-12.5	19.5
J022051.9-045832	Ultra	0.043873	190.9	189.1	16.5	173.5	60	3	-28.9	6.1
J022056.9-045917	Ultra	0.075589	323.5	345.9	26.3	299.0	32	7	81.7	16.7
J022058.7-051320	Deep	0.064971	279.6	291.4	22.9	256.9	52	3	25.0	2.9
J022110.7-050630	Deep	0.041315	180.0	177.9	15.7	164.1	70	2	-45.1	1.4
J022117.8-045040	Ultra	0.043552	189.5	187.8	16.4	172.5	54	4	-73.3	3.0
J022138.1-052631	Deep	0.006912	30.6	25.9	4.6	25.5	66	4	49.6	2.5
J022145.5-050210	Deep	0.073552	315.2	335.4	25.7	291.0	57	5	-85.4	3.7
J022236.8-043432	Deep	0.069496	298.4	314.9	24.4	275.3	75	3	28.6	0.8
J022300.8-043408	Deep	0.073381	314.4	334.5	25.6	290.3	43	9	46.6	11.9
J022332.2-044928	Deep	0.044673	194.3	192.9	16.7	176.7	55	10	28.1	23.2
J022338.7-042431	Deep	0.068655	294.9	310.5	24.1	271.9	45	7	59.2	12.1
J022350.6-045045	Deep	0.044031	191.5	190.1	16.5	174.4	71	5	-18.2	15.2
J022357.0-051918	Deep	0.07593	324.9	347.7	26.4	300.3	30	12	-78.0	24.0
J022358.3-050756	Deep	0.052276	226.4	227.2	18.9	205.2	59	4	-45.9	5.3
J022400.9-044943	Deep	0.044032	191.5	190.1	16.5	174.4	63	3	-85.0	5.2
J022429.6-044037	Deep	0.044031	191.5	190.1	16.5	174.4	85	5	20.6	0.5
J022443.4-045158	Deep	0.040994	178.6	176.8	15.6	163.2	51	5	26.1	14.6
J022522.7-045519	Deep	0.036864	160.9	151.1	13.9	140.5	74	4	-29.2	1.5

[a] Cosmological luminosity distance [b] Flow model based luminosity distance [c] Angular diameter distance from flow model

Table A.2. Surface brightness photometry values in the g band.

Name	A_g	m_g	e(m_g)	$\mu_{0,g}$	e($\mu_{0,g}$)	$\overline{\mu}_{eff,g}$	e($\overline{\mu}_{eff,g}$)	n_g	e(n_g)	$r_{\mathrm{eff},g}$	e($r_{\mathrm{eff},g}$)	$R_{\mathrm{eff},g}$	e($R_{\mathrm{eff},g}$)
MGTH_	mag	mag		mag arcsec^{-2}		mag arcsec^{-2}				arcsec		kpc	
J021534.4-042904	0.067	22.54	0.01	25.35	0.24	25.99	0.02	0.70	0.09	1.95	0.11	3.39	0.54
J021625.5-044228	0.067	20.68	0.00	23.80	0.22	24.38	0.04	0.67	0.08	2.20	0.10	1.98	0.31
J021642.0-044221	0.065	19.24	0.02	23.50	0.38	25.40	0.07	1.44	0.16	6.80	0.52	6.12	1.03
J021645.4-042035	0.069	19.79	0.04	24.01	0.17	25.16	0.08	1.01	0.07	4.73	0.16	8.38	1.29
J021714.5-052922	0.077	17.87	0.00	23.00	0.14	24.00	0.04	0.93	0.05	6.71	0.16	2.28	0.35
J021724.3-043322	0.066	21.15	0.01	24.58	0.08	25.30	0.05	0.75	0.02	2.69	0.08	1.90	0.29
J021759.3-041634	0.069	17.66	0.08	23.29	0.42	24.81	0.15	1.23	0.17	10.71	1.31	7.41	1.44
J021808.2-045217	0.067	21.74	0.00	25.11	0.12	25.77	0.01	0.72	0.05	2.56	0.07	1.33	0.20
J021818.0-043234	0.066	20.21	0.01	22.71	0.22	24.60	0.04	1.44	0.09	3.02	0.10	2.74	0.42
J021848.1-045028	0.067	19.57	0.01	24.03	0.14	24.91	0.09	0.85	0.04	4.67	0.21	8.30	1.30
J021934.4-042846	0.073	21.94	0.01	22.10	0.51	23.64	0.01	1.24	0.22	0.87	0.07	1.27	0.22
J022011.5-051047	0.071	21.83	0.00	24.83	0.07	25.29	0.01	0.58	0.02	1.96	0.03	2.15	0.32
J022026.3-045912	0.073	20.40	0.00	23.70	0.27	25.03	0.05	1.12	0.11	3.36	0.21	3.01	0.49
J022029.4-041207	0.066	18.50	0.01	23.48	0.14	24.69	0.05	1.05	0.05	6.89	0.21	2.84	0.43
J022042.1-052115	0.075	19.02	0.02	22.97	0.36	24.52	0.04	1.25	0.15	5.02	0.28	0.74	0.12
J022045.0-050058	0.075	21.11	0.01	23.41	0.58	25.25	0.01	1.41	0.24	2.69	0.28	4.70	0.86
J022051.9-045832	0.078	20.30	0.01	24.45	0.10	25.29	0.02	0.83	0.04	3.97	0.08	3.68	0.56
J022056.9-045917	0.077	22.25	0.00	24.30	0.11	25.24	0.02	0.89	0.05	1.58	0.04	2.51	0.38
J022058.7-051320	0.073	21.87	0.01	24.00	0.19	24.65	0.03	0.71	0.08	1.43	0.05	1.93	0.30
J022110.7-050630	0.069	21.33	0.02	24.30	0.23	25.04	0.05	0.77	0.09	2.20	0.10	1.89	0.30
J022117.8-045040	0.072	20.41	0.01	23.22	0.20	24.50	0.03	1.09	0.08	2.63	0.09	2.42	0.37
J022138.1-052631	0.082	17.28	0.01	24.01	0.10	24.47	0.09	0.58	0.02	10.94	0.42	1.51	0.23
J022145.5-050210	0.073	20.78	0.01	23.21	0.18	24.33	0.06	0.99	0.08	2.05	0.06	3.15	0.48
J022236.8-043432	0.081	20.53	0.00	23.55	0.09	24.36	0.06	0.82	0.03	2.33	0.07	3.38	0.52
J022300.8-043408	0.089	20.34	0.02	23.34	0.35	23.83	0.13	0.60	0.13	1.99	0.15	3.06	0.51
J022332.2-044928	0.084	18.84	0.04	23.26	0.41	24.88	0.25	1.29	0.13	6.46	1.01	6.11	1.33
J022338.7-042431	0.087	20.96	0.00	23.85	0.21	24.60	0.06	0.78	0.08	2.13	0.10	3.05	0.48
J022350.6-045045	0.086	18.05	0.15	23.71	0.39	25.58	0.16	1.42	0.16	12.76	1.06	11.92	2.05
J022357.0-051918	0.08	20.45	0.02	23.81	0.44	25.51	0.09	1.33	0.18	4.12	0.39	6.57	1.17
J022358.3-050756	0.085	20.93	0.01	24.52	0.06	25.07	0.03	0.64	0.02	2.68	0.05	2.97	0.45
J022400.9-044943	0.087	20.34	0.00	24.06	0.06	24.82	0.04	0.78	0.02	3.13	0.06	2.93	0.44
J022429.6-044037	0.082	19.25	0.20	24.82	0.77	25.60	0.73	0.80	0.06	7.44	2.05	6.94	2.18
J022443.4-045158	0.094	20.36	0.02	23.90	0.16	24.96	0.06	0.96	0.06	3.32	0.13	2.82	0.44
J022522.7-045519	0.093	18.98	0.00	23.46	0.15	24.95	0.10	1.21	0.04	6.24	0.30	4.76	0.75

Table A.3. Surface brightness photometry values in the *r* band.

Name MGTH_	A_r mag	m_r mag	e(m_r) mag	$\mu_{0,r}$ mag arcsec^{-2}	e($\mu_{0,r}$) mag arcsec^{-2}	$\overline{\mu}_{eff,r}$ mag arcsec^{-2}	e($\overline{\mu}_{eff,r}$) mag arcsec^{-2}	n_r	e(n_r)	$r_{\mathrm{eff},r}$ arcsec	e($r_{\mathrm{eff},r}$) arcsec	$R_{\mathrm{eff},r}$ kpc	e($R_{\mathrm{eff},r}$) kpc
J021534.4-042904	0.047	21.70	0.01	24.35	0.05	24.88	0.03	0.63	0.02	1.72	0.02	2.99	0.45
J021625.5-044228	0.046	20.42	0.00	23.52	0.22	24.13	0.04	0.69	0.09	2.21	0.10	1.99	0.31
J021642.0-044221	0.045	18.95	0.02	23.01	0.41	25.04	0.07	1.51	0.18	6.58	0.47	5.92	0.98
J021645.4-042035	0.048	19.39	0.04	23.72	0.18	25.03	0.09	1.11	0.06	5.35	0.21	9.49	1.47
J021714.5-052922	0.053	17.55	0.00	22.49	0.14	23.71	0.04	1.06	0.06	6.83	0.17	2.33	0.35
J021724.3-043322	0.046	20.76	0.00	24.14	0.10	24.94	0.05	0.81	0.03	2.74	0.07	1.94	0.30
J021759.3-041634	0.048	17.26	0.08	22.72	0.49	24.31	0.15	1.27	0.20	10.22	1.24	7.07	1.37
J021808.2-045217	0.046	21.47	0.01	24.85	0.16	25.56	0.01	0.75	0.06	2.62	0.09	1.36	0.21
J021818.0-043234	0.045	20.14	0.01	22.62	0.30	24.61	0.05	1.49	0.13	3.12	0.14	2.83	0.44
J021848.1-045028	0.046	19.26	0.00	23.54	0.16	24.54	0.10	0.93	0.05	4.56	0.21	8.10	1.27
J021934.4-042846	0.05	21.50	0.01	21.61	0.84	23.37	0.02	1.36	0.36	0.94	0.12	1.37	0.27
J022011.5-051047	0.049	21.53	0.01	24.49	0.09	25.00	0.01	0.62	0.03	1.97	0.04	2.17	0.33
J022026.3-045912	0.05	20.13	0.00	23.37	0.20	24.65	0.05	1.09	0.08	3.19	0.17	2.86	0.45
J022029.4-041207	0.046	18.16	0.02	23.00	0.13	24.39	0.04	1.16	0.05	7.03	0.23	2.89	0.44
J022042.1-052115	0.052	18.54	0.02	22.71	0.28	24.24	0.04	1.24	0.12	5.52	0.27	0.82	0.13
J022045.0-050058	0.052	20.89	0.01	23.09	0.45	24.76	0.01	1.31	0.19	2.36	0.19	4.13	0.70
J022051.9-045832	0.054	19.79	0.01	24.09	0.11	24.90	0.01	0.81	0.04	4.20	0.09	3.90	0.59
J022056.9-045917	0.053	21.67	0.01	23.50	0.14	24.58	0.03	0.98	0.06	1.53	0.04	2.43	0.37
J022058.7-051320	0.051	21.25	0.02	22.93	0.45	23.96	0.01	0.94	0.19	1.39	0.10	1.87	0.31
J022110.7-050630	0.048	21.10	0.02	23.93	0.24	24.88	0.05	0.90	0.09	2.27	0.13	1.95	0.31
J022117.8-045040	0.05	20.17	0.00	23.04	0.17	24.16	0.04	1.00	0.07	2.52	0.08	2.32	0.36
J022138.1-052631	0.057	16.90	0.01	23.65	0.10	24.13	0.09	0.60	0.02	11.18	0.43	1.55	0.24
J022145.5-050210	0.05	20.55	0.01	22.56	0.18	23.95	0.07	1.16	0.08	1.91	0.07	2.95	0.46
J022236.8-043432	0.056	20.17	0.00	22.82	0.10	23.81	0.06	0.92	0.03	2.12	0.06	3.08	0.47
J022300.8-043408	0.062	20.11	0.01	22.97	0.09	23.59	0.07	0.69	0.02	1.98	0.07	3.05	0.47
J022332.2-044928	0.058	18.45	0.05	22.78	0.34	24.51	0.23	1.35	0.10	6.52	0.81	6.17	1.20
J022338.7-042431	0.06	20.69	0.00	23.36	0.15	24.20	0.06	0.83	0.05	2.01	0.08	2.88	0.45
J022350.6-045045	0.059	17.89	0.14	23.33	0.44	25.23	0.18	1.44	0.18	11.74	1.11	10.96	1.94
J022357.0-051918	0.055	20.20	0.02	22.93	0.40	25.14	0.06	1.61	0.17	3.87	0.30	6.18	1.04
J022358.3-050756	0.059	20.76	0.01	24.21	0.06	24.79	0.03	0.66	0.02	2.55	0.05	2.82	0.43
J022400.9-044943	0.06	20.00	0.00	23.51	0.08	24.39	0.04	0.85	0.03	3.02	0.07	2.82	0.43
J022429.6-044037	0.057	18.87	0.17	24.25	0.80	25.16	0.75	0.87	0.07	7.22	2.32	6.74	2.39
J022443.4-045158	0.065	20.01	0.02	23.33	0.15	24.57	0.07	1.07	0.05	3.26	0.14	2.77	0.43
J022522.7-045519	0.064	18.66	0.01	22.95	0.14	24.48	0.09	1.23	0.04	5.82	0.27	4.44	0.70

Table A.4. Surface brightness photometry values in the *i* band.

Name	A_i	m_i	e(m_i)	$\mu_{0,i}$	e($\mu_{0,i}$)	$\overline{\mu}_{eff,i}$	e($\overline{\mu}_{eff,i}$)	n_i	e(n_i)	$r_{\mathrm{eff},i}$	e($r_{\mathrm{eff},i}$)	$R_{\mathrm{eff},i}$	e($R_{\mathrm{eff},i}$)
MGTH_	mag	mag		mag arcsec^{-2}		mag arcsec^{-2}				arcsec		kpc	
J021534.4-042904	0.035	21.21	0.00	23.63	0.14	24.40	0.03	0.79	0.06	1.73	0.05	3.01	0.46
J021625.5-044228	0.034	20.26	0.00	23.35	0.13	23.93	0.04	0.66	0.05	2.16	0.07	1.94	0.30
J021642.0-044221	0.033	18.83	0.03	22.30	0.34	24.87	0.06	1.80	0.14	6.44	0.42	5.81	0.95
J021645.4-042035	0.035	19.39	0.04	23.50	0.18	24.81	0.10	1.11	0.06	4.85	0.21	8.60	1.34
J021714.5-052922	0.039	17.35	0.01	22.21	0.13	23.50	0.04	1.10	0.05	6.77	0.16	2.31	0.35
J021724.3-043322	0.034	20.59	0.00	23.86	0.08	24.71	0.06	0.84	0.02	2.66	0.08	1.88	0.29
J021759.3-041634	0.036	17.07	0.04	22.29	0.33	24.11	0.11	1.40	0.13	10.21	0.76	7.07	1.18
J021808.2-045217	0.034	21.30	0.00	24.63	0.10	25.38	0.01	0.77	0.04	2.61	0.07	1.36	0.21
J021818.0-043234	0.034	20.15	0.01	22.49	0.32	24.59	0.05	1.54	0.14	3.08	0.15	2.79	0.44
J021848.1-045028	0.034	19.10	0.01	23.21	0.15	24.25	0.11	0.95	0.04	4.27	0.23	7.58	1.21
J021934.4-042846	0.037	21.24	0.00	21.67	0.30	22.94	0.01	1.09	0.12	0.87	0.04	1.27	0.20
J022011.5-051047	0.036	21.38	0.00	24.31	0.15	24.90	0.01	0.67	0.06	2.02	0.07	2.22	0.34
J022026.3-045912	0.037	19.96	0.00	23.09	0.23	24.48	0.05	1.15	0.09	3.20	0.18	2.88	0.46
J022029.4-041207	0.034	18.10	0.02	22.86	0.12	24.19	0.04	1.12	0.04	6.60	0.21	2.72	0.42
J022042.1-052115	0.039	18.40	0.02	22.76	0.18	24.01	0.04	1.08	0.08	5.28	0.19	0.78	0.12
J022045.0-050058	0.039	20.76	0.00	22.78	0.43	24.40	0.01	1.29	0.18	2.13	0.15	3.73	0.62
J022051.9-045832	0.04	19.57	0.01	23.91	0.11	24.66	0.02	0.78	0.04	4.16	0.09	3.87	0.59
J022056.9-045917	0.04	21.34	0.00	23.12	0.19	24.26	0.03	1.01	0.08	1.54	0.05	2.44	0.37
J022058.7-051320	0.038	20.97	0.01	22.99	0.25	23.80	0.02	0.81	0.11	1.47	0.06	1.98	0.31
J022110.7-050630	0.036	21.02	0.01	24.06	0.15	24.83	0.04	0.79	0.06	2.30	0.10	1.97	0.31
J022117.8-045040	0.037	20.09	0.00	22.78	0.18	23.95	0.03	1.03	0.07	2.36	0.07	2.17	0.33
J022138.1-052631	0.042	16.73	0.01	23.47	0.11	23.97	0.09	0.61	0.02	11.17	0.48	1.55	0.24
J022145.5-050210	0.037	20.42	0.01	22.71	0.11	23.74	0.06	0.95	0.04	1.84	0.06	2.84	0.44
J022236.8-043432	0.042	19.90	0.00	22.90	0.09	23.77	0.07	0.85	0.02	2.37	0.08	3.44	0.53
J022300.8-043408	0.046	19.75	0.08	22.47	0.55	23.78	0.14	1.11	0.23	2.56	0.34	3.93	0.79
J022332.2-044928	0.043	18.25	0.06	22.68	0.29	24.28	0.22	1.27	0.07	6.41	0.78	6.07	1.17
J022338.7-042431	0.045	20.41	0.00	23.39	0.07	24.04	0.05	0.71	0.02	2.12	0.06	3.04	0.46
J022350.6-045045	0.044	17.79	0.18	23.22	0.48	25.01	0.20	1.38	0.20	11.09	1.34	10.36	1.99
J022357.0-051918	0.041	19.92	0.03	22.77	0.27	24.88	0.05	1.55	0.11	3.92	0.23	6.25	1.01
J022358.3-050756	0.043	20.71	0.01	24.26	0.08	24.75	0.03	0.60	0.03	2.56	0.06	2.83	0.43
J022400.9-044943	0.045	19.78	0.01	23.44	0.08	24.27	0.04	0.83	0.03	3.16	0.08	2.95	0.45
J022429.6-044037	0.042	18.65	0.18	24.08	0.83	25.03	0.77	0.90	0.09	7.51	2.44	7.01	2.51
J022443.4-045158	0.048	19.90	0.08	23.41	0.43	24.41	0.15	0.93	0.17	3.19	0.35	2.71	0.51
J022522.7-045519	0.048	18.53	0.00	22.86	0.13	24.34	0.09	1.20	0.04	5.78	0.25	4.41	0.69

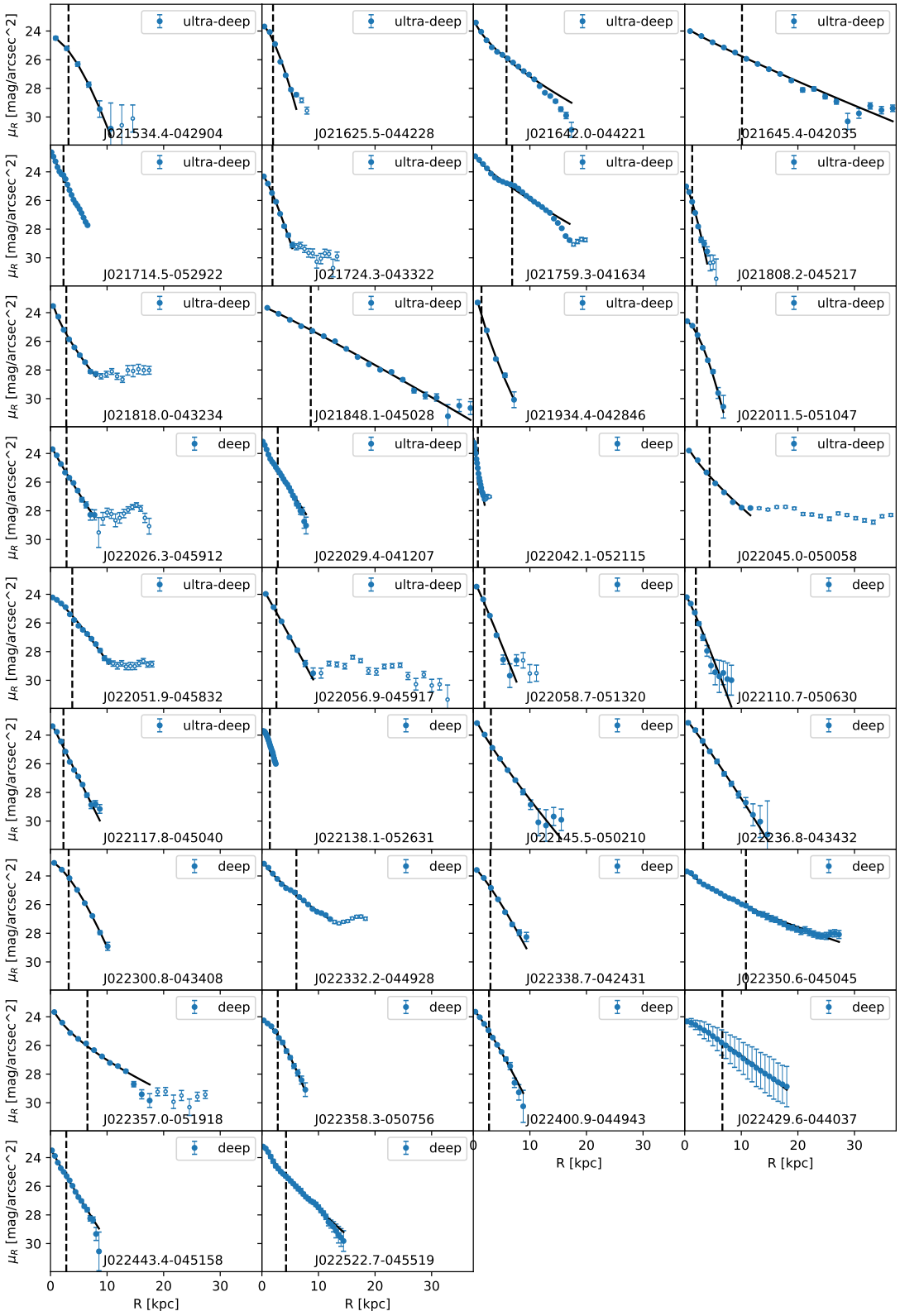

Fig. A.1. Surface brightness profiles of all 34 candidate LSBGs selected from the MIGHTEE ES H I catalog. Blue circles with error bars correspond to the galaxy profiles extracted from the images, solid black lines show the resulting Sérsic fit, and vertical dashed black lines denote the effective radius obtained from the fit.

Appendix B: HI spectra of optically identified LSBGs

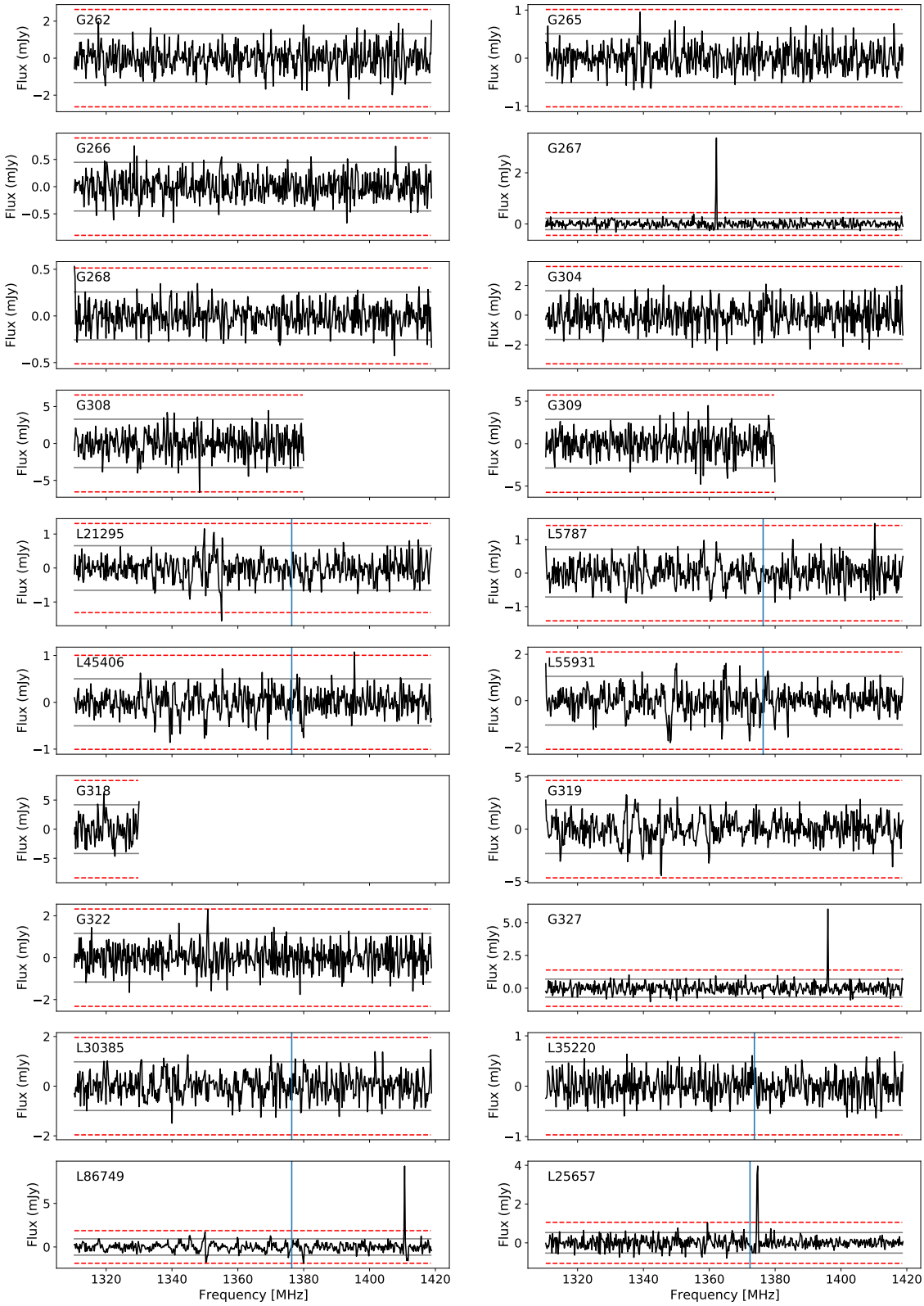

Fig. B.1. H I spectra for every optically identified galaxy. Solid gray horizontal lines indicate ±2 times the standard deviation in the spectra, and the dashed red lines indicate ±4 times the standard deviation. For the L23 galaxies, the optical redshift of the assigned host galaxy is indicated by the blue lines. The G18 galaxies have no redshift information available.